

Controlling the Dynamics of a Single Atom in Lateral Atom Manipulation

Joseph A. Stroscio* and Robert J. Celotta

We studied the dynamics of a single cobalt (Co) atom during lateral manipulation on a copper (111) surface in a low-temperature scanning tunneling microscope. The Co binding site locations were revealed in a detailed image that resulted from lateral Co atom motion within the trapping potential of the scanning tip. Random telegraph noise, corresponding to the Co atom switching between hexagonal close-packed (hcp) and face-centered cubic (fcc) sites, was seen when the tip was used to try to position the Co atom over the higher energy hcp site. Varying the probe tip height modified the normal copper (111) potential landscape and allowed the residence time of the Co atom in these sites to be varied. At low tunneling voltages (less than ~ 5 millielectron volts), the transfer rate between sites was independent of tunneling voltage, current, and temperature. At higher voltages, the transfer rate exhibited a strong dependence on tunneling voltage, indicative of vibrational heating by inelastic electron scattering.

Manipulation of single atoms and molecules on surfaces with the use of a scanning tunneling microscope (STM) (1) encompasses lateral processes, which transfer atoms and molecules parallel to the surface, as well as vertical processes, which transfer atoms and molecules between the tip and surface (2). Lateral atom manipulation experiments (1, 3, 4) and theory (5, 6) have focused on the importance of the tunable chemical bond interaction between the tip and adatom, whereas vertical manipulation experiments (7, 8) and theory (9–12) stress the importance of inelastic electron tunneling in stimulating atom transfer via vibrational excitation of the adatom-substrate bond. Vibrational excitation induced by tunneling electrons has also been used to induce rotations of single molecules (13).

We report a study of the dynamics of a single metal atom during lateral manipulation. We first discuss the dynamics of the manipulated Co atom in the context of a novel type of STM image—which we refer to as a “manipulated atom” image—that reveals the binding sites of the substrate. This image is obtained by the rastering of a Co atom over the Cu(111) surface, using the tip-induced local potential to trap the Co atom under the rastering probe tip. We then study the dynamics of the manipulated Co

atom, which switches between neighboring (and almost equivalent) fcc and hcp sites of the Cu(111) surface at cryogenic temperatures. This switching appears as a periodic noise pattern in the manipulated atom images and as telegraph noise in tunnel current measurements. Measurements of the atom transfer rate as a function of tunneling current and tip height show the importance of vibrational excitation via inelastic electron tunneling in lateral atom manipulation. We demonstrate detailed control of single-atom switching by tuning the local potential landscape with the tip-adatom interaction. The control we can obtain suggests the development of sophisticated procedures to facilitate bond-breaking and greatly enhance lateral atom manipulation processes.

Listening to atoms move. We studied the lateral manipulation of a Co atom residing on a single-crystal Cu(111) surface (Fig. 1A) (14). On this surface, the fcc site has no Cu atom below it in the lower Cu layer and, as a consequence, is energetically favored over the hcp site as a binding site for Co (15, 16).

Imaging with the STM typically places the probe tip sufficiently far from the sample so that tip-sample interactions do not initiate atomic movement. To move a Co adatom (fig. S1A) (17), we first bring the tip closer to the adatom by adjusting the tunneling junction resistance R (R is set by the ratio of the tunneling voltage V to the tunneling current I). This interaction creates a highly localized potential well that traps the adatom under the tip (2). For simple point-to-point

adatom repositioning, the STM tip first moves laterally to the adatom while at the greater tip height Z used in normal STM imaging, where Z is the relative distance between the STM probe tip and the surface of the substrate. The STM then traps the adatom by decreasing R (decreasing Z), moves the tip laterally while maintaining I constant, and finally releases the adatom at the destination by reverting to the value of R used in normal imaging (increasing Z). As shown by Bartels *et al.* (3), recording Z while repositioning an adatom provides a measure of how well the adatom is following the tip motion.

The underlying atomic lattice is needed as a template to construct nanostructures by atom manipulation, but for the Cu(111) surface, it cannot be observed in a conventional tip height image (fig. S1A) (17) because of the very small electron lattice corrugation. We therefore devised what we call a manipulated atom image as a way to observe substrate lattice structure. We form this image by rastering the tip over the surface in the normal topographic imaging mode, except now with a Co adatom trapped in the moving tip-induced potential well that exists at lower R values (Fig. 2A) (fig. S1B) (17). Details, on a lateral scale of a fraction of a lattice constant, are visible in this manipulated atom image that cannot be seen in the normal STM image, even when such images are taken at the lower R values (fig. S1C) (17). The difference is that in a manipulated atom image, the trapped Co atom can move laterally relative to the tip in response to the local potential surface; this motion is recorded as changes in Z , because the STM servo is trying to maintain I constant. Using the motion of the Co atom to image the local binding sites is an example of a new class of measurements based on single-atom transducers sensing their local environments; we refer to this as “atom-based metrology.”

Surprisingly, the manipulated atom image (Fig. 2A) shows three-fold symmetry with three distinct features, labeled A, B, and C, which is only possible if more than the top layer is contributing to the imaging process. At first glance, this image looks like a replica of the surface model of Cu(111) shown in Fig. 1A. However, a detailed analysis reveals that the binding site of Co on Cu(111) is always at the site labeled A in Fig. 2A in our low-temperature STM measurements. This fact—together with manipulated atom image measurements of Co on Cu(111) with different tips with various resolving functions, as well as atom-manipulation simulations (6)—indicates that the feature at A is an image of a

Electron Physics Group, National Institute of Standards and Technology, Gaithersburg, MD 20899-8412, USA.

*To whom correspondence should be addressed.
E-mail: joseph.stroscio@nist.gov

stationary Co adatom at the fcc site (15, 16). The Co atom remains stationary in the fcc site as the tip begins to move laterally (Fig. 1C); a lateral force begins to develop as the tip continues to move away from the Co atom (Fig. 1D). When the lateral force becomes large enough, the Co atom hops to the nearest binding site within the trapping range of the tip (Fig. 1E). This switching motion produces the manipulated atom image in Fig. 2A. This switching is unlike the so-called sliding mode of atom manipulation (2, 4, 6) in which the adatom follows exactly the tip motion at sufficiently low R . Instead, the Co atom does not precisely follow the tip (over the tunneling resistance range of 50 to 180 kilohms), but hops to the fcc or hcp binding site nearest the moving tip.

The maximum Z is roughly the same at the center of features A and B in Fig. 2A. Therefore, we assign feature B to Co in the hcp site, as one would expect from the geometric similarity of the fcc and hcp sites (Fig. 1A), which leaves the on-top site for assignment to feature C. Feature C is lower than features A and B, because the Co atom is unstable on the on-top site and switches to the nearest fcc site (site A in Fig. 2A), and the tip height decreases in response. This tip motion is borne out by simulations (6) and is similar to that observed in experiments of the manipulation of Ag atoms on Ag(111) (4). For these measurement conditions, the manipulated atom image can be thought of as a binding site image for Co on Cu(111). Note that in the manipulated atom images, site B, the hcp site, is noisy (Fig. 2A). This speckle suggests that a dynamic process is occurring at the hcp site during atom manipulation.

Audio-frequency components of the tunneling current have been monitored with an audio system and used as a real-time diagnostic of the atom manipulation process (18). The origin of such “sounds” in the tunneling current during atom manipulation has remained largely unexplored. In our work, an audio-frequency modulation of the tunneling current can be “heard” as a manipulated atom image is recorded (movie S1) (17). An examination of the tunneling current signal shows that the noise density increases when the Co atom is positioned over the hcp sites (Fig. 2B). It is this increase in current noise that gives rise to the “sound” of atom manipulation when the tunneling current is used to provide audio feedback.

To measure the current noise, we measured the time dependence of I (19) at the hcp site during a manipulated atom image, as in Fig. 2A. The tip position was held fixed at a selected lateral location on the surface by pausing the raster, and the tip height was fixed by disabling the STM servo. The tunneling signal was measured as a function

of time for several values of V . After the measurement, the STM servo was turned back on and the raster was continued until another selected position was reached. The time dependence of I at two different locations (Fig. 3A) near the center of the hcp site is shown in Fig. 3, B and D. Random two-state telegraph noise, switching between a high level of ~ 35 nA and a low level of ~ 23 nA in Fig. 3B, results from the Co atom

switching between the hcp site under the tip location and the nearest fcc site, labeled as #1 in Fig. 3A. The corresponding tunneling current distribution (Fig. 3C) shows that, for the choice of interaction parameters used in this measurement, the Co atom spends most of its time in the fcc site. The measurement in Fig. 3B was obtained at a location ~ 0.2 Å away from the center of the hcp site. Only two states were observed because the tip-

Fig. 1. (A) Top view of the Cu(111) surface with the Co adatom shown in its natural fcc binding site. (B) Schematic potential well for the Co atom in fcc and hcp sites: blue curve, native potential well, no tip-Co interaction; green curve, tip-induced potential well; red curve, native potential with added tip-induced potential. The potential at the hcp site increases in depth because of the increase in tip-Co interaction as the tip-Co distance decreases. The tip-induced potential well over the hcp site causes the Co atom to switch between the fcc and hcp sites, producing discrete changes in the tunnel current. (C to E) Schematic of manipulated atom tip height trace. Initially, with the tip over the fcc site, the force on the Co atom is vertical and the tip images the Co atom. As the tip moves down the side of the Co atom, a lateral force develops (D). When the tip reaches the hcp site, the lateral force is large enough to induce the Co atom to hop to the hcp site (E). The green curve is the measured tip height trace from the manipulated atom image in Fig. 2A.

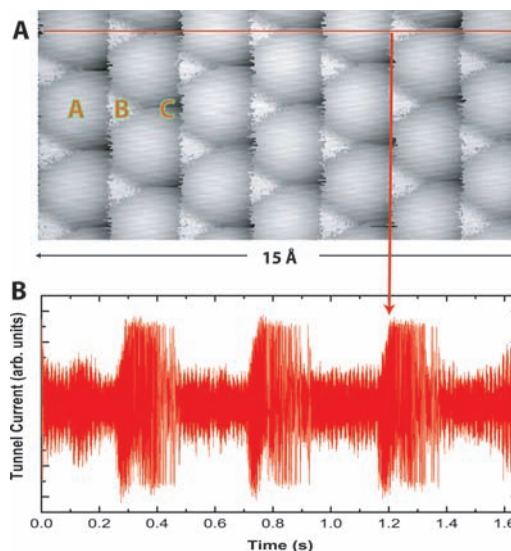
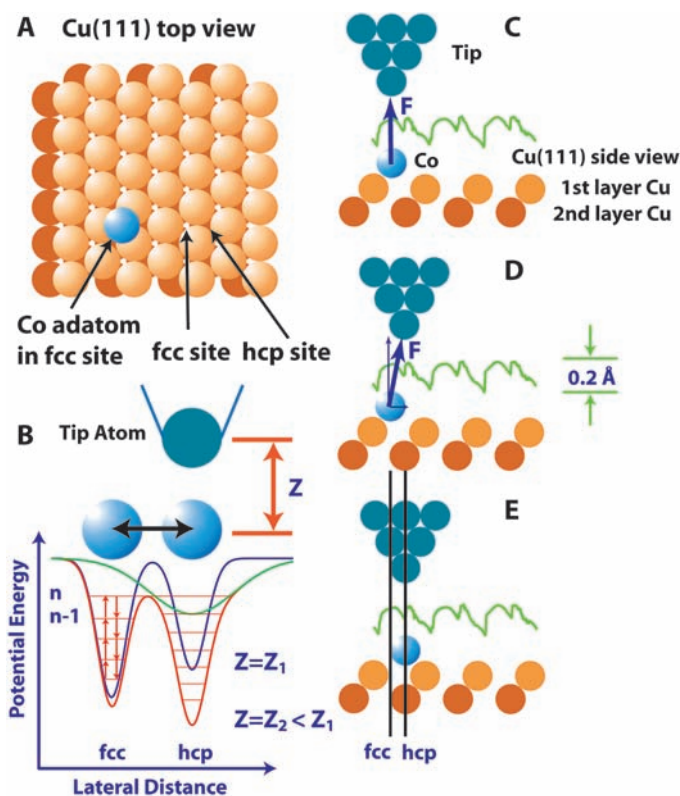


Fig. 2. (A) Manipulated atom image of Co over Cu(111) surface. Tunnel current, 50 nA; sample bias, -5 mV; $T = 4.3$ K. The labels A, B, and C denote fcc, hcp, and top sites, respectively. (B) Tunnel current recorded during manipulated atom image going through the hcp and fcc sites as indicated by the horizontal line in (A). The arrow shows the increased noise in the tunnel current corresponding to the position of the hcp site.

induced potential well is closest to the fcc site labeled #1 in Fig. 3A.

When the tip was positioned closer to the center of the hcp site (Fig. 3D), we observed four different levels in I corresponding to the Co atom switching between the hcp site and all three neighboring fcc sites. In the I distribution (Fig. 3E), a single high current level corresponds to the Co atom in the hcp site, but the lower I level splits into three sublevels corresponding to the fcc sites labeled #1 to #3. Note that the current

transitions are always between the hcp level and an fcc level, and never between two fcc levels directly.

The data in Fig. 3 show that the tip-Co atom interaction modifies the unperturbed multiwell surface potentials, as shown schematically in Fig. 1B. Because we observed atom switching only with the tip at close tip-Co atom distances (low tunneling resistances), we can conclude that the original potential well at the fcc site is deeper than the original well at the hcp site, consistent

with previous experiments and calculations (15, 16). The presence of the tip-Co atom interaction deepens the potential well at the hcp site (Fig. 1B), which makes it favorable for the Co atom to switch back and forth at these temperatures. The residence times for each state can be varied from being predominantly at the fcc site to being predominantly at the hcp site by varying the strength of the tip-Co atom interaction. We next consider the exact mechanisms of atom switching for the case of an ideal double-well potential.

An ideal two-state fluctuator. Two-state fluctuating systems are fundamental in the theory of $1/f$ noise in solids (20, 21), but in many of these systems the exact identity of the two-state object is unknown. Here, we can use the STM probe tip to modify the potential landscape to create a known two-state fluctuating system on the basis of the position of a single atom.

Figure 3F shows random two-state telegraph noise, with its associated current distribution shown in Fig. 3G, for a measurement obtained at a tunneling voltage of 8.4 mV. The transitions are about an order of magnitude more frequent than in Fig. 3, B and C, where V was 3.3 mV. We examined this difference quantitatively by determining the average transition rate for the Co atom to switch sites from hcp to fcc, R_{hcp} , and from fcc to hcp, R_{fcc} . The Co atom has no memory of the time it spent at a given site; therefore, these events can be described by a two-state discrete Markov process with an exponentially distributed residence time probability density given by

$$P_{\text{hcp, fcc}}(t) = R_{\text{hcp, fcc}} \exp(-R_{\text{hcp, fcc}} t) \quad (1)$$

(20). The residence time distributions for the hcp and fcc sites (fig. S2, A and B) (17) are well described by an exponential distribution, in agreement with Eq. 1. The transition rates were determined to be 184.6 ± 3.0 Hz and 568 ± 8.6 Hz (22) for the hcp and fcc sites, respectively, for the tunneling parameters used in the measurement.

The transfer rates for the two-state fluctuator, corresponding to a double-well potential of the hcp and fcc sites and measured at constant Z , span four orders of magnitude as the voltage is varied from 1 to 15 mV, which corresponds to a current variation of ~ 5 to 100 nA (Fig. 4) [see movie S2 to listen to audio recordings of this single-atom switching (17)]. The transfer rates are nearly symmetrical with tunneling voltage polarity and are characterized by two distinct regimes. For voltage magnitudes less than ~ 5 mV, the transfer rate is relatively independent of V followed by a crossover to a regime strongly dependent on V . This behavior is seen in all our measurements, irrespective of tunneling resistance, temperature, or tip used.

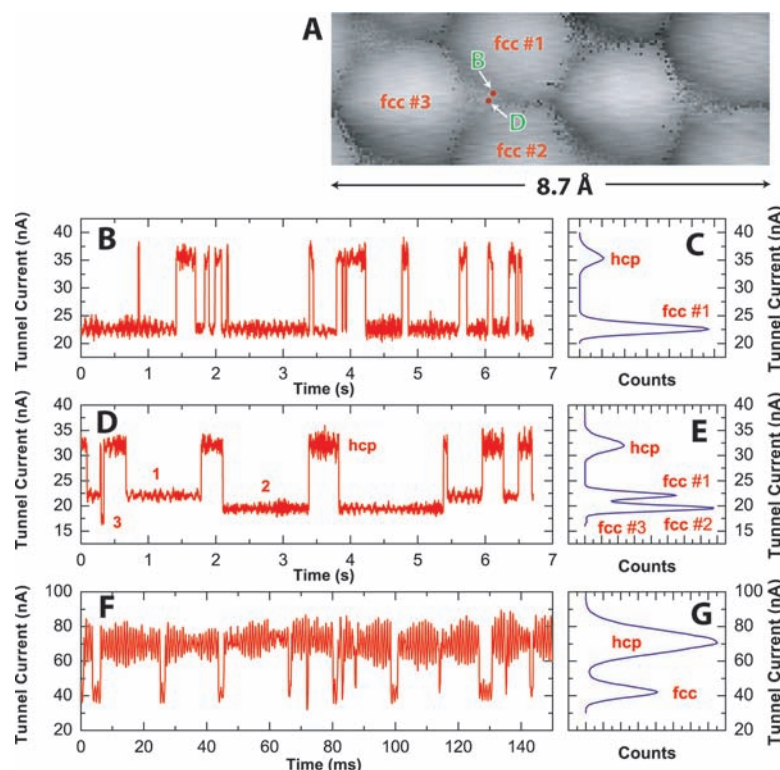
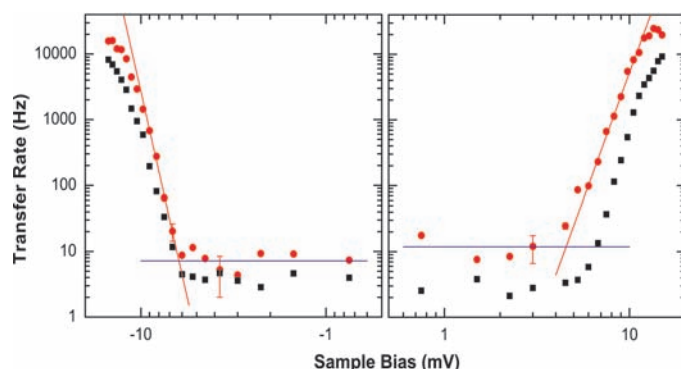


Fig. 3. (A) Co manipulated atom image on Cu(111). Tunnel current, 100 nA; sample bias, 11.0 mV; junction resistance, 110 kilohms; $T = 2.3$ K. (B and D) Tunnel current versus time measurements recorded at the positions indicated by the corresponding red spots in (A) near the hcp site. Sample bias, 3.3 mV. (C and E) The corresponding histograms of the current distributions. (F) Tunnel current versus time measurement showing two-state random telegraph noise near the hcp site for Co on Cu(111) measurement at junction resistance of 120 kilohms. Sample bias, 8.4 mV; $T = 2.3$ K. (G) Corresponding histogram of the current distribution.

Fig. 4. Transfer rate versus sample bias at constant tip height, obtained by measuring the distribution of residence time in the hcp and fcc states from two-state random telegraph noise in the tunnel current. Junction resistance = 150 kilohms; $T = 2.3$ K. R_{hcp} , red circles; R_{fcc} , black squares. Solid red line shows a power-law fit to the initial threshold region; blue horizontal line shows the average transfer rate for the low-bias region for the hcp transfer rate.



A model for the atom switching observed in Fig. 4 can be based on the theory developed to explain the vertical Xe atom switch experiment by Eigler *et al.* (7). A vibrational heating mechanism (9–11) was invoked to reproduce the power-law dependence observed in the Xe switch experiment. With vibrational heating, the atom overcomes the potential barrier through stepwise climbing of a vibrational ladder of the adatom-substrate bond excitations (Fig. 1B) through a competition between gaining energy from inelastic tunneling electrons and losing energy to electron-hole pairs and phonons. Gao *et al.* (12) showed that the power-law behavior results from an Arrhenius-like expression for the transfer rate,

$$R_{\text{VH}} \approx n\Gamma_{\uparrow} \exp[-(\tilde{V}_{\text{B}}/k_{\text{B}}T_{\text{v}})] \quad (2)$$

where Ω is 2π times the vibrational frequency, \tilde{V}_{B} is defined as $(n-1)\hbar\Omega$ (which is close to the actual barrier height V_{B}), n is the number of vibrational levels in the well with spacing $\hbar\Omega$, Γ_{\uparrow} and Γ_{\downarrow} are the vibrational excitation and deexcitation rates between nearest neighbor levels of the harmonic oscillator potential (which contain a thermal contribution and a contribution due to inelastic electron tunneling), k_{B} is Boltzmann's constant, and \hbar is Planck's constant divided by 2π . Because of the nonthermal population of the vibrational system excited through inelastic electron tunneling, the vibrational temperature $T_{\text{v}} = (\hbar\Omega/k_{\text{B}})[\ln(\Gamma_{\uparrow}/\Gamma_{\downarrow})]^{-1}$ can be higher than the substrate temperature T . This model yields a transfer rate $R \propto I^n$ or V^n , because I and V are linearly related by the junction resistance. At lower I and V values, a crossover to a thermally activated regime is predicted (12) but has not been observed experimentally.

The transfer rate data in Fig. 4 do not follow a pure power law, varying as V^n , as predicted by the vibrational heating models. We found an initial fast turn-on of the transfer rate (Fig. 4). Fitting a power law to the hcp transfer rates for voltages between -7 and -9 mV gives an exponent of 12.5 ± 1.2 (22) (solid red line in Fig. 4). At higher V , the power-law behavior is followed by a gradual decrease in slope. In the vibrational heating model, deviations from a pure power law are expected when the inelastic tunneling rate, I_{in}/e , is comparable to the vibrational relaxation rate, γ . For our experiment, this crossover should occur at a total current of about 100 nA, taking $\gamma \approx 10^{10} \text{ s}^{-1}$ (12, 23) and the inelastic tunneling current to be 1% of the total current. This is approximately where we observe deviations from a pure power law (Fig. 4). Such deviations can also result from a number of competing paths for the barrier crossing, as discussed by Walkup *et al.* (10).

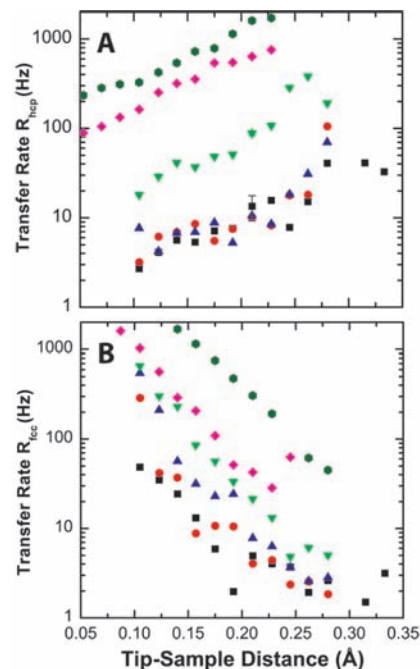
For applied potentials within ~ 5 meV of the Fermi energy, we observed a finite

background rate of atom switching in the range of 1 to 20 Hz that is independent of tunneling voltage and current (Fig. 4). Two possible mechanisms for this transfer are thermal activation and quantum tunneling of the Co atom between the hcp and fcc sites. For thermal activation, a very strong variation of the transfer rate would be expected over the temperature range from 2 to 4 K (fig. S3A) (17), assuming preexponential factors corresponding to typical vibrational frequencies ranging from 10^{10} to 10^{13} Hz. However, the measurements shown in fig. S3, A and B (17) show relatively little variation in the transfer rate with T , requiring an alternate explanation.

Although quantum tunneling might seem improbable given the large mass of the Co atom, atomic-scale distances together with a barrier height less than ~ 50 meV can result in appreciable tunneling rates for large-mass atoms (24, 25). The rate for quantum tunneling can be estimated with the Wentzel-Kramer-Brillouin (WKB) approximation,

$$R_{\text{QT}} = \nu \exp\{-d(2mV_{\text{B}})^{1/2}/\hbar\} \quad (3)$$

(26), where ν is on the order of the vibrational frequency, d is an effective distance between wells, m is the mass of the Co atom, and V_{B} is the potential barrier. With the barrier estimated from calculations (15), $V_{\text{B}} = 37$ meV, $\nu = 10^{12} \text{ s}^{-1}$, and $d = 0.75$ Å (27), we estimate a transfer rate of 30 Hz, which is comparable to the rate seen in our measurements for low V and supports the quantum tunneling mechanism for atom transfer in this regime.



Zero tip-sample distance corresponds to the initial set point at junction resistance of 90 kilohms; $Z = 0.35$ Å corresponds to 180 kilohms (fig. S4). Sample bias, -5 mV; $T = 2.3$ K.

Controlling atom dynamics. To gauge the importance of the tip-adatom interaction on the adatom dynamics, we varied the probe tip height Z at a constant V . For this measurement, we created a two-state fluctuator by pausing during a manipulated atom image when the Co atom was in the vicinity of the hcp site. At this location, while tunneling at the resistance used for the manipulated atom image, we turned the STM servo off to allow direct control of Z . We then recorded time sequence data of the tunneling current at a series of Z values set by positioning the tip with a calibrated piezo transducer.

As we increased Z , we expected a weaker tip-Co interaction to create a shallower potential well at the hcp site (Fig. 1B). An increase in Z corresponds to an increase in R and a reduction in I (fig. S4). The transfer rates, computed from the tunneling current time sequence data, depend strongly on Z both in the quantum tunneling and vibrational heating regimes (Fig. 5, A and B). The hcp rates (Fig. 5A) increased with Z , whereas the fcc rates (Fig. 5B) showed a similar decrease. The increases in the hcp rates may at first seem surprising, because the current is decreasing with Z and the transfer rate due to vibrational heating is a strong function of I . The explanation lies in the even stronger effect of the changes in the local potential energy surface, which leads to an increase in the transfer rate that overcomes the decrease in the transfer rate due to vibrational heating over the range of tip heights used in this measurement.

A series of current histograms plotted as a function of the tip height (Fig. 5C) shows

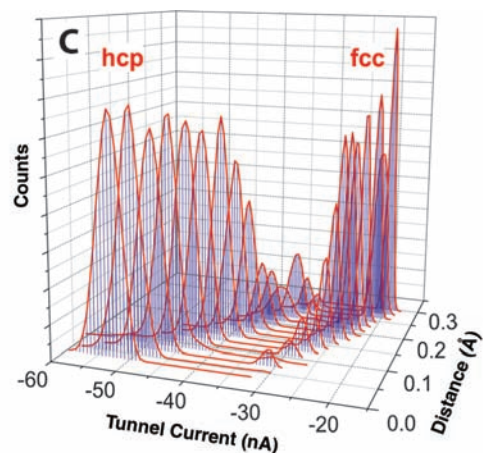


Fig. 5. (A) hcp transfer rate, (B) fcc transfer rate versus tip-sample distance at constant sample bias. Black squares, sample bias $V = -5$ mV; red circles, $V = -6$ mV; blue triangles, $V = -7$ mV; green inverted triangles, $V = -8$ mV; magenta diamonds, $V = -9$ mV; green circles, $V = -10$ mV. (C) Current distribution from two-state telegraph noise obtained near the hcp site during a Co manipulated atom measurement as a function of tip-sample distance.

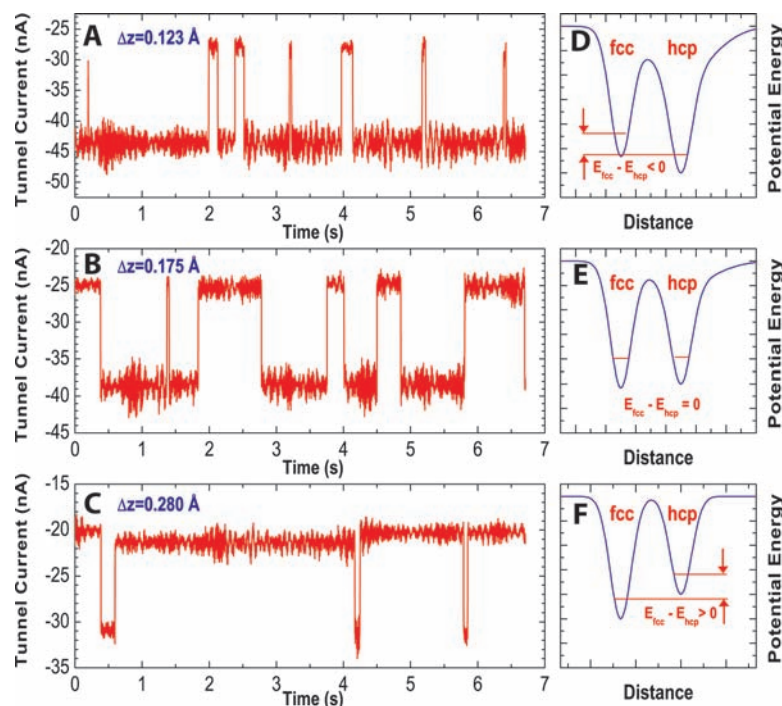


Fig. 6. Telegraph noise measurements near the hcp site during a Co manipulated atom measurement as a function of tip-sample distance. Tip-sample distance was increased (A) 0.123 Å, (B) 0.175 Å, and (C) 0.280 Å relative to the initial set point at junction resistance of 90 kilohms. Sample bias, -5 mV; $T = 2.3$ K. Corresponding current histogram distributions for these data are shown in Fig. 5C. (D to F) Schematic potential diagrams showing the relative variation of the potentials that give rise to the change in duty cycle between the hcp and fcc signals observed in (A) to (C).

that at low R the Co atom can be completely trapped in the hcp site. As Z is increased and the tip-adatom interaction weakens, the hcp population continuously decreases and the fcc population increases. Finally, at the largest Z the Co atom resides at the fcc site. Thus, the tip-adatom potential is strong enough to completely reverse the relative binding energy of the fcc and hcp sites (Fig. 6). Snapshots of the two-state telegraph noise are shown in Fig. 6, A to C, for the circumstances where the hcp potential is deeper than, approximately equal to, and higher than the fcc potential.

The difference in energy between the hcp-site and fcc-site ground states, schematically shown in Fig. 6, D to F, can be obtained from the measured transfer rates at low voltage (Fig. 5, A and B) by using the detailed balance condition

$$R_{\text{fcc}} = \exp[-(E_{\text{fcc}} - E_{\text{hcp}})/k_{\text{B}}T]R_{\text{hcp}} \quad (4)$$

(12). Figure 7 shows the energy difference, which varies linearly with tip height with a slope of 6.5 ± 0.9 meV/Å (22). The data in Figs. 6 and 7 reflect an induced 2-meV shift in the relative energies of the hcp and fcc ground states. Although this corresponds to only a 5% variation of the 37-meV potential well depth (15), it is sufficient to completely reverse the binding characteristics of the two sites. This conveniently allows us to tune the

atom switching to an appropriate time scale for observation and to “listen” to the atom dynamics within the audio range.

Conclusions. We have separately studied the two most important factors in atom manipulation: vibrational heating of the adatom-substrate bond and the tip-adatom interaction. We see how the tip-adatom potential effectively constrains the Co atom to within a nearest neighbor distance of the tip position. The tip-adatom interaction can be tuned to distort the potential surface and control the atom’s dynamics. The vibrational excitation acts effectively to raise the atom within its potential well, bringing it closer to the activation barrier for transfer between sites. Control of the two independent processes of vibrational heating and guiding the adatom by tuning the potential landscape with the tip-adatom interaction can greatly enhance lateral atom manipulation processes and their applicability.

We believe the ability to control the transfer of a single atom between lattice sites can lead to the ability to switch and control electrical signals in atomic-scale devices built by atom manipulation. This capability expands on the concept of the atomic switch first discovered by Eigler *et al.* (7), where in the original geometry the atom switches vertically between the sample and tip. In a lateral atom switch, the metal

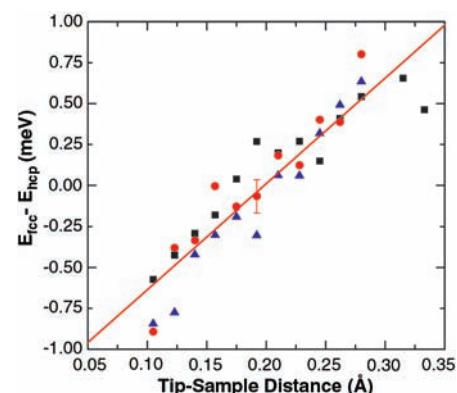


Fig. 7. Energy difference between the hcp and fcc potentials obtained from the detailed balance expression in Eq. 4, using the transfer rates for the hcp and fcc sites as a function of tip-sample distance. $T = 2.3$ K. The symbols correspond to separate measurements at different sample bias: squares, $V = -5$ mV; circles, $V = -6$ mV; triangles, $V = -7$ mV. The solid line is a linear fit to all three data sets.

atom can remain bound to the substrate, which allows it to control conductance through atomic-scale devices. A number of different atomic-scale devices can be realized given the ability to control a lateral single-atom switch (28). Of course, there are difficult challenges to overcome, such as extending these concepts to semiconductor substrates where the potential corrugations are larger, before the control of electrical conductance with this type of atomic switch is possible.

References and Notes

1. D. M. Eigler, E. K. Schweizer, *Nature* **344**, 524 (1990).
2. J. A. Stroscio, D. M. Eigler, *Science* **254**, 1319 (1991).
3. L. Bartels, G. Meyer, K.-H. Rieder, *Phys. Rev. Lett.* **79**, 697 (1997).
4. S. W. Hla, K.-F. Braun, K.-H. Rieder, *Phys. Rev. B* **67**, 201402 (2003).
5. X. Bouju, C. Joachim, C. Girard, *Phys. Rev. B* **59**, R7845 (1999).
6. A. Kühnle, G. Meyer, S. W. Hla, K.-H. Rieder, *Surf. Sci.* **499**, 15 (2002).
7. D. M. Eigler, C. P. Lutz, W. E. Rudge, *Nature* **352**, 600 (1991).
8. T. C. Shen *et al.*, *Science* **268**, 1590 (1995).
9. S. Gao, M. Persson, B. I. Lundqvist, *Solid State Commun.* **84**, 271 (1992).
10. R. E. Walkup, D. M. Newns, Ph. Avouris, *Phys. Rev. B* **48**, 1858 (1993).
11. M. Brandbyge, P. Hedegård, *Phys. Rev. Lett.* **72**, 2919 (1994).
12. S. Gao, M. Persson, B. I. Lundqvist, *Phys. Rev. B* **55**, 4825 (1997).
13. B. C. Stipe, M. A. Rezaei, W. Ho, *Science* **280**, 1732 (1998).
14. This system was realized experimentally as follows: A Cu(111) sample was cleaned by repeated cycles of Ne sputtering and annealing to 600°C while reflection high-energy electron diffraction was used to monitor sample quality. We then transferred the substrate, along with an Ir probe tip prepared using a field ion microscope, to a low-temperature STM. Co adatoms were then deposited onto the Cu(111) substrate at 7 K. All preparation, transfers, and measurements took place in an ultrahigh-vacuum system containing a low-temperature STM of our design that operates over a temperature range of 2.3 to 4.3 K.

15. D. V. Tsivlin, V. S. Stepanyuk, W. Hergert, J. Kirschner, *Phys. Rev. B* **68**, 205411 (2003).
16. V. S. Stepanyuk et al., *Phys. Rev. B* **68**, 205410 (2003).
17. Video clips and additional data are available on Science Online.
18. Although we know of no mention in the published literature, we believe D. M. Eigler was the first to use the tunnel current for audio feedback during atom manipulation.
19. We measured the time dependence of I at the hcp site as a function of V at fixed Z , and as a function of Z at fixed V , during atom manipulation. These two measurements are interrelated through the tunnel junction relation (and elucidate different aspects of the switching dynamics), where, at low voltages, $I = V/R$, at fixed Z , and $I = A \exp(-2\kappa Z)$, for fixed V ; here, κ is the tunneling barrier decay constant. See (29).
20. Sh. Kogan, in *Electronic Noise and Fluctuations in Solids* (Cambridge Univ. Press, Cambridge, 1996).
21. M. B. Weissman, *Rev. Mod. Phys.* **60**, 537 (1988).
22. Errors reported in this article represent two standard deviations of the statistical uncertainty in the measurement.
23. B. N. J. Persson, *Phys. Rev. B* **44**, 3277 (1991).
24. A. J. Heinrich, C. P. Lutz, J. A. Gupta, D. M. Eigler, *Science* **298**, 1381 (2002).
25. J. Repp, G. Meyer, K.-H. Rieder, P. Hyldgaard, *Phys. Rev. Lett.* **91**, 206102 (2003).
26. L. D. Landau, E. M. Lifshitz, in *Quantum Mechanics* (Pergamon, New York, ed. 3, 1977).
27. We take the effective distance to be half the fcc-hcp distance for a constant barrier approximation that would yield the same WKB barrier integral.
28. Y. Wada, *Optoelectronics Devices Technol.* **10**, 205 (1995).
29. J. A. Stroscio, W. J. Kaiser, Eds., *Scanning Tunneling Microscopy*, vol. 27 of *Methods of Experimental Physics* (Academic Press, Boston, 1993).
30. We thank A. Fein and S. Blankenship for their assistance, and W. Gadzuk, M. Stiles, and N. Zimmerman for very fruitful discussions. Supported in part by the Office of Naval Research.

Supporting Online Material
www.sciencemag.org/cgi/content/full/1102370/DC1
Figs. S1 to S4
Movies S1 and S2

6 July 2004; accepted 25 August 2004
Published online 9 September 2004;
10.1126/science.1102370
Include this information when citing this paper.

Rescue of Cardiac Defects in *Id* Knockout Embryos by Injection of Embryonic Stem Cells

Diego Fraidenaich,¹ Elizabeth Stillwell,¹ Elizabeth Romero,¹ David Wilkes,³ Katia Manova,² Craig T. Basson,³ Robert Benezra^{1*}

We report that *Id* knockout mouse embryos display multiple cardiac defects, but mid-gestation lethality is rescued by the injection of 15 wild-type embryonic stem (ES) cells into mutant blastocysts. Myocardial markers altered in *Id* mutant cells are restored to normal throughout the chimeric myocardium. Intraperitoneal injection of ES cells into female mice before conception also partially rescues the cardiac phenotype with no incorporation of ES cells. Insulin-like growth factor 1, a long-range secreted factor, in combination with WNT5a, a locally secreted factor, likely account for complete reversion of the cardiac phenotype. Thus, ES cells have the potential to reverse congenital defects through *Id*-dependent local and long-range effects in a mammalian embryo.

The *Id* proteins are dominant negative antagonists of basic helix-loop-helix (bHLH) transcription factors and regulate differentiation in multiple lineages (1). Previous studies have shown that *Id1* to *Id4* are expressed in embryonic tissues during development in partially overlapping patterns (2) and that *Id1* and *Id3* are detected at mid-gastrulation in the three germ layers (3). In the developing heart, *Id1* to *Id3* are detected in the endocardial cushion (EC) mesenchyme from embryonic day 10.5 (E10.5) through E16.5 (2), but *Id4* is absent (2). Here, we show that *Id1* to *Id3* are also expressed in the epicardium and endocardium but are absent in the myocardium [fig. S1, A to C, for *Id1*; fig. S1, D and E, for *Id3*; (4) for *Id2*]. *Id1* to *Id3* expression becomes confined to the leaflets of the cardiac valves as the atrio-

ventricular (AV) EC tissue myocardializes (4). *Id1* and *Id3* expression persists in the cardiac valves, endocardium, endothelium, and epicardium at postnatal day 7 (P7) (4).

Double- and triple-*Id* knockout embryos display severe cardiac defects and die at mid-gestation. *Id1*, *Id2*, or *Id3* knockout (KO) embryos do not exhibit developmental abnormalities, but ablation of two *Id* genes in any combination (*Id1/Id2*, *Id2/Id3*, or *Id1/Id3*) leads to embryonic lethality by E13.5 (table S1). *Id1/Id3* KO embryos display a collapse of brain vasculature with associated hemorrhage and enhanced expression of p16 and bHLH neural factors in the neighboring neuroepithelium by E12 or E13 (5). We wanted to identify the cause of embryonic lethality common to all KO embryos. Embryos lacking four or five copies of *Id1*, *Id2*, and *Id3* displayed multiple cardiac abnormalities at E11.5 to E13.5 (Fig. 1, A, B, D, E, G, H, J, K, M, and N for *Id1^{-/-}Id3^{-/-}*; fig. S2C for *Id1^{-/-}Id2^{-/-}*; fig. S2D for *Id1^{-/-}Id2^{+/-}Id3^{-/-}*; and fig. S2F for *Id1^{+/-}Id2^{+/-}Id3^{-/-}*). Embryo size was reduced by 10 to 30%. KO embryos displayed ventricular septal defects (VSDs)

associated with impaired ventricular trabeculation and thinning of the compact myocardium. Trabeculae had disorganized sheets of myocytes surrounded by discontinuous endocardial cell lining. Cell proliferation in the myocardial wall was defective [percentage 5-bromo-2'-deoxyuridine (BrdU) \pm SD: wild type (WT): $38 \pm 4\%$; *Id1^{-/-}Id3^{-/-}*: $23 \pm 3\%$; (Fig. 1, J to L and L inset)]. Outflow tract (OT) atresia was apparent (Fig. 1, M and N). OT and AV ECs displayed low cellularity at E11.5, which resulted in hypoplastic ECs in *Id1^{+/-}Id2^{+/-}Id3^{-/-}* embryos at E13.5 (fig. S2, E and F). The epicardium appeared normal, and EC apoptosis was unaffected [terminal deoxynucleotidyl transferase-mediated deoxyuridine triphosphate nick end labeling (4)]. The impaired development of the myocardium in *Id* KO animals even though *Id*s are not expressed there suggests that *Id*s might participate in molecular signaling between myocardium and the *Id⁺* epicardium, endocardium, and EC. Alternatively, loss of *Id* expression in early myocardial precursors might lead to myocardial defects.

Id1/Id2/Id3 KO embryos have severe cardiac malformation as early as E9.5 (fig. S2, A and B). The overall size of the embryo and heart was reduced by 40 to 60%. The atrium did not separate from the ventricle, and ventricular trabeculation was rudimentary (fig. S2, A and B). No hemorrhage was observed in *Id1/Id2/Id3* KO brains at E9.5 (4). No triple-KO embryos survived to E11.5 (table S1). These observations suggest that a defective heart is the primary cause of mid-gestation lethality.

Injection of ES cells into *Id* KO blastocysts corrects cardiac defects and rescues embryonic lethality. Cardiac defects and embryonic lethality was reversed by injecting 15 β -galactosidase (*LacZ*)-marked ES Rosa 26 (R26) cells into *Id* KO blastocysts. In the resultant embryos, *LacZ*-positive cells were detected in the heart and forebrain (Fig. 1C). At E11.5, all cardiac structures in rescued embryos were identical to those of WT embryos. No endocardial, myocardial, or EC defects were observed (Fig. 1, C, F, I, L, and O) (4), and cell proliferation was restored [percentage BrdU in compact myo-

¹Cancer Biology and Genetics Program, ²Molecular Cytology Core Facility, Memorial Sloan-Kettering Cancer Center, ³Molecular Cardiology Laboratory, Greenberg Cardiology Division, Department of Medicine, Weill Medical College of Cornell University, New York, NY 10021, USA.

*To whom correspondence should be addressed. E-mail: r-benezra@ski.mskcc.org